AAAS
Research
Volume 2019, Article ID 8174314, 9 pages
https://doi.org/10.34133/2019/8174314

Research Article

Fast Cryomediated Dynamic Equilibrium Hydrolysates towards Grain Boundary-Enriched Platinum Scaffolds for Efficient Methanol Oxidation

Chao Zhang,[1] **Huajie Huang**,[2] **Jianan Gu**,[1] **Zhiguo Du**,[1] **Bin Li**,[1] **Songmei Li**,[1] **and Shubin Yang**[1]

[1]*Key Laboratory of Aerospace Advanced Materials and Performance of Ministry of Education, School of Materials Science and Engineering, Beihang University, 100191 Beijing, China*
[2]*College of Mechanics and Materials, Hohai University, Nanjing 210098, China*

Correspondence should be addressed to Songmei Li; songmei_li@buaa.edu.cn and Shubin Yang; yangshubin@buaa.edu.cn

Received 15 May 2019; Accepted 24 July 2019; Published 13 October 2019

Although platinum nanocrystals have been considered as potential electrocatalysts for methanol oxidation reaction (MOR) in fuel cells, the large-scale practical implementation has been stagnated by their limited abundance, easy poisoning, and low durability. Here, grain boundary-enriched platinum (GB-Pt) scaffolds are produced in large scale via facilely reducing fast cryomediated dynamic equilibrium hydrolysates of platinum salts. Such plentiful platinum grain boundaries are originated from the fast fusion of short platinum nanowires during reduction of the individually and homogeneously dispersed platinum intermediates. These grain boundaries can provide abundant active sites to efficiently catalyze MOR and meanwhile enable to oxidize the adsorbed poisonous CO during the electrocatalytic process. As a consequence, the as-synthesized GB-Pt scaffolds exhibit an impressively high mass activity of 1027.1 mA mg_{Pt}^{-1} for MOR, much higher than that of commercial Pt/C (345.2 mA mg_{Pt}^{-1}), as well as good stability up to 5000 cycles. We are confident that this synthetic protocol can be further extended to synthesize various grain boundary-enriched metal scaffolds with broad applications in catalysis.

1. Introduction

Direct methanol fuel cells (DMFCs) have been demonstrated as one of the most promising power sources for electronic mobile devices and electric vehicles due to their ultrahigh energy densities and low pollution [1–3]. However, their wide applications have stagnated owing to the notoriously sluggish kinetics of methanol oxidation reaction (MOR) at the anode [4–8]. Thus, it is inevitable to develop high active precious metal electrocatalysts like platinum (Pt) to reduce the energy barriers of MOR [9–11]. From the perspective of Pt atomic efficiency [12], the precisely controlled synthesis of Pt nanocrystals such as Pt irregular nanoparticles [13, 14], nanowires [15–18], and nanorods [19] is highly desirable since they have inherent anisotropic morphologies with abundant low-coordinated surface atoms [20, 21], enabling to slow down the ripening process and increase the electrocatalytic activities for methanol oxidation.

Very recently, it is demonstrated that Pt nanocrystals with twin defects or dislocations have shown unique electrocatalytic behaviors for methanol oxidation, differentiating from coarsely gained grains, single crystals, or particles [21–23], since Pt atoms close to defects have decreased the number of neighbors in the first coordination shell, and are favorable to forcefully adsorb the reactants and catalyze related bond-breaking reactions during the catalytic process [24, 25]. Thus, the emergence of abundant defects, dislocations, or grain boundaries not only reduce the activation energy for methanol oxidation but also afford abundant catalytic sites for the oxidation of the adsorbed CO intermediate, significantly improving their stabilities [26, 27]. Hence, there is great interest in Pt nanocrystals with a high density of grain boundaries for electrocatalytic MOR [20, 26]. Unfortunately, to date, it remains a big challenge to synthesize grain boundary-enriched Pt nanocrystals via a facile and cost-efficient approach [28, 29].

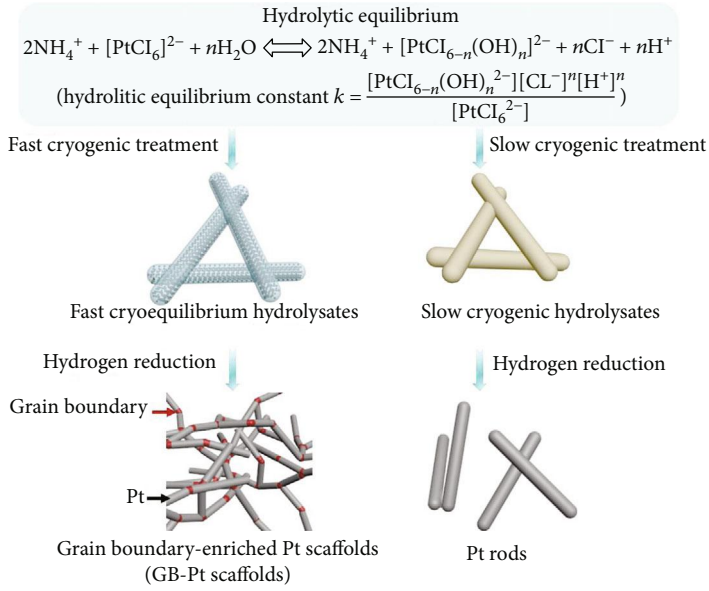

Figure 1: Schematic illustration of the synthesis of 3D GB-Pt scaffolds. The procedure for preparing 3D GB-Pt scaffolds involves two steps: (1) fast cryogenic treatment of the $(NH_4)_2PtCl_6$ solution to produce fast cryogenic hydrolysates; (2) hydrogen reduction of the obtained fast cryogenic hydrolysates.

Here, 3D grain boundary-enriched Pt scaffolds (3D GB-Pt scaffolds) are facilely produced via reducing fast cryogenic hydrolysates of ammonium hexachloroplatinate ($(NH_4)_2PtCl_6$) aqueous solution. These grain boundaries are originated from the rapid coalescence of short Pt nanowires (~13.2 nm) during reduction of the individually and homogeneously dispersed platinum hydrolysates. These grain boundaries can provide abundant active sites to efficiently catalyze MOR and meanwhile enable to oxidize the adsorbed poisonous CO during the electrocatalytic process. Coupled to the 3D interconnected networks, both mass transport and electron transfer during MOR are fast in 3D GB-Pt scaffolds. As a consequence, the as-synthesized 3D GB-Pt scaffolds show an ultrahigh mass activity of 1027.1 mA mg_{Pt}^{-1} for MOR, much higher than that of commercial Pt/C (345.2 mA mg_{Pt}^{-1}), and long-term durability up to 5000 cycles (only 9.8% loss of the initial activity).

2. Results

2.1. Preparation of 3D GB-Pt Scaffolds. As illustrated in Figure 1 and Figure S1, 3D GB-Pt scaffolds were synthesized through reduction of fast cryogenic hydrolysates of platinum salts in aqueous solution. Specifically, $(NH_4)_2PtCl_6$ (5 mg) was dissolved in 10 ml deionized water, forming a pale-yellow solution. After standing for 10 h, the hydrolysis of $(NH_4)_2PtCl_6$ reaches a dynamic equilibrium as follows [30, 31]:

$$2NH_4^+ + [PtCl_6]^{2-} + nH_2O \rightleftharpoons 2NH_4^+ + [PtCl_{6-n}(OH)_n]^{2-} + nCl^- + nH^+ \quad (1)$$

where the hydrolysis equilibrium could be adjusted via tuning the pH values and the concentration of Cl^- during the hydrolysis process (Figure S2). After fast cryogenic treatment (the treatment temperature is -196°C), a yellow foam with equilibrium hydrated $[PtCl_{6-n}(OH)_n]^{2-}$, NH_4^+, Cl^-, and nonhydrolytic $[PtCl_6]^{2-}$ was formed. Then, the foam was reduced at 200°C under a mixed gas of H_2 and Ar with a v/v ratio of 1 : 9 for 2 h, affording 3D GB-Pt scaffolds. In contrast, Pt rods were generated through reduction of the slow cryogenic hydrolysates, since hydrolytic equilibrium of $(NH_4)_2PtCl_6$ went reversely back during the slow cryogenic process.

2.2. Effect of Fast Dynamic Equilibrium Hydrolysates to Guide 3D GB-Pt Scaffold Formation. To identify the dynamic equilibrium hydrolysates of $(NH_4)_2PtCl_6$ during our fast cryogenic treatment, UV-vis absorption measurement was conducted owing to its high sensitivity to ligand-to-metal ($Cl^- \rightarrow Pt$) charge transfer of $[PtCl_6]^{2-}$ and $[PtCl_{6-n}(OH)_n]^{2-}$ complexes [32, 33]. In principle, by adjusting the pH values of $(NH_4)_2PtCl_6$ solution from 0 to 12, the different dynamic equilibriums could be achieved, as demonstrated by their UV-vis absorption spectra with different absorbance intensities at ~262 nm (Figure 2(a)), which were originated from the charge transfer involving orbitals with Cl ligand π-character [30, 33]. Notably, while adjusting the pH value to 14, all the $(NH_4)_2PtCl_6$ was conversed to $[Pt(OH)_6]^{2-}$, Cl^-, and NH_4^+, where the hydrolytic equilibrium was completely broken [34]. Through fast cryogenic treatment, the hydrolysates at the different dynamic equilibrium states could be well maintained. This could be clearly demonstrated via their UV-vis absorption spectra (Figure 2(b)). On the contrary, through slow cryogenic treatment (the treatment temperature is -5°C), all the adsorption bands of the hydrolysates at the different dynamic equilibrium states showed the similar absorption intensities (Figure 2(c)). It is suggested

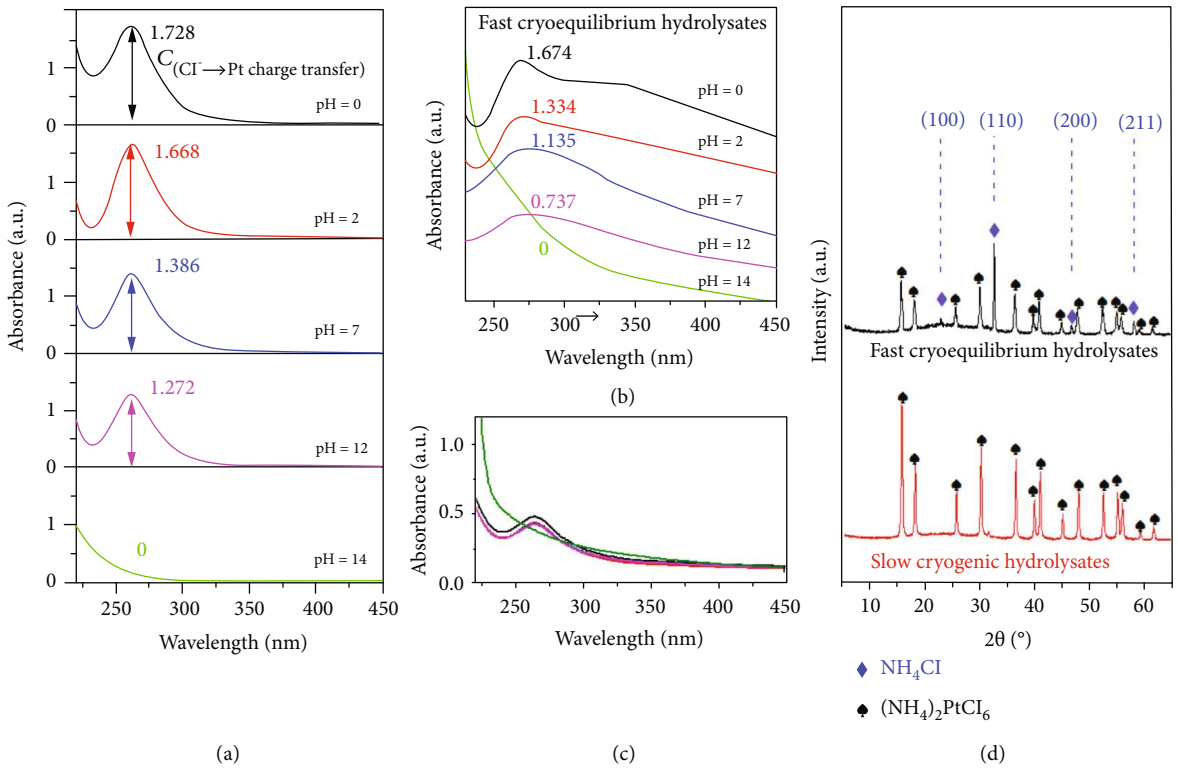

FIGURE 2: Detailed structural characterizations of fast and slow cryogenic hydrolysates. (a) UV-vis absorption spectra of $(NH_4)_2PtCl_6$ aqueous solutions (0.1 mg ml^{-1}) with different pH values (from 0 to 14), clearly indicating that the $[PtCl_6]^{2-}$ ion undergoes deep hydrolysis with increasing pH values. (b, c) UV-vis adsorption spectra of fast cryoequilibrium hydrolysates (b) and slow cryogenic hydrolysates (c) obtained from the $(NH_4)_2PtCl_6$ solution with different pH values (from 0 to 14), showing that the hydrolysates at the different dynamic equilibrium states could be well maintained through fast cryogenic treatment. (d) XRD patterns of fast cryoequilibrium hydrolysates and slow cryogenic hydrolysates confirm the existence of NH_4Cl in the obtained fast cryoequilibrium hydrolysates.

that the different levels of hydrolysate $[PtCl_{6-n}(OH)_n]^{2-}$ were recrystallized to $(NH_4)_2PtCl_6$ during our slow cryogenic process.

To further evaluate the crystalline phases of fast cryogenic intermediates, X-ray diffraction (XRD) measurement was conducted and is shown in Figure 2(d). Interestingly, in the case of fast cryogenic intermediates, except for the characterization peaks of $(NH_4)_2PtCl_6$, there are four additional XRD peaks detected at 22.9°, 32.6°, 46.9°, and 58.3° (marked with blue diamonds in Figure 2(d)), indexed to (100), (110), (200), and (211) planes of NH_4Cl (JCPDS no. 72-2378), respectively. The typical TEM (Figure S3a-f) and elemental mapping images (shown in Figure S4) reveal that the product NH_4Cl behaves like a matrix to accommodate the homogeneous dispersion of the fast cryogenic Pt-containing intermediates with sizes of 3-5 nm. Hence, through initial hydrogen reduction treatment, numerous individual Pt nanocrystalline structures could be produced, derived from Pt-containing intermediates. Meanwhile, NH_4Cl would be gradually decomposed and leave gaps between the Pt nanocrystalline structures. With further increase of the reduction time, such gaps allow the infusion between adjacent Pt nanocrystalline structures, generating grain boundary-enriched Pt scaffolds as demonstrated in Figure 3 and Figures S5 and S6. The typical TEM images (Figure 3(b)–3(e) and Figure S7) clearly disclose that these scaffolds are constructed from short Pt crystalline wires with average lengths of ~13 nm and diameters of ~4.2 nm. HRTEM images (Figures 3(d) and 3(e) and Figure S8) show clearly the grain boundaries between two short Pt wires and an obvious interlayer spacing of 0.223 nm, corresponding to $d(111)$ of Pt [35, 36]. In contrast, different levels of hydrolysate $[PtCl_{6-n}(OH)_n]^{2-}$ and Cl^- were recrystallized to single-crystalline $(NH_4)_2PtCl_6$ during the slow cryogenic treatment, without the detection of equilibrium products of the hydrolysis (Figure 2(d) and Figure S9). After hydrogen reduction treatments of slow cryogenic intermediates, only Pt rods were obtained (Figures S10 and S11). This may be ascribed to the low level of NH_4Cl in the slow cryogenic intermediates, which are unable to prevent the fast growth of big Pt crystalline structures. Moreover, pH values of the $(NH_4)_2PtCl_6$ solution also affect the formation of 3D GB-Pt scaffolds. As shown in Figures S12 and S13, while the pH value is 2 and 7, the resultant GB-Pt scaffolds show interconnected 3D networks. As the pH value is 0, all the nanowires or particles are strongly aggregated, owing to the less amount of the hydrolysis product NH_4Cl, which cannot efficiently prevent the aggregation during reduction process. In contrast, as the pH value arrives to 12 and 14, all the Pt nanocrystalline structures are separated, without formation of good networks. This should be ascribed to the excessive hydrolysis product NH_4Cl after fast

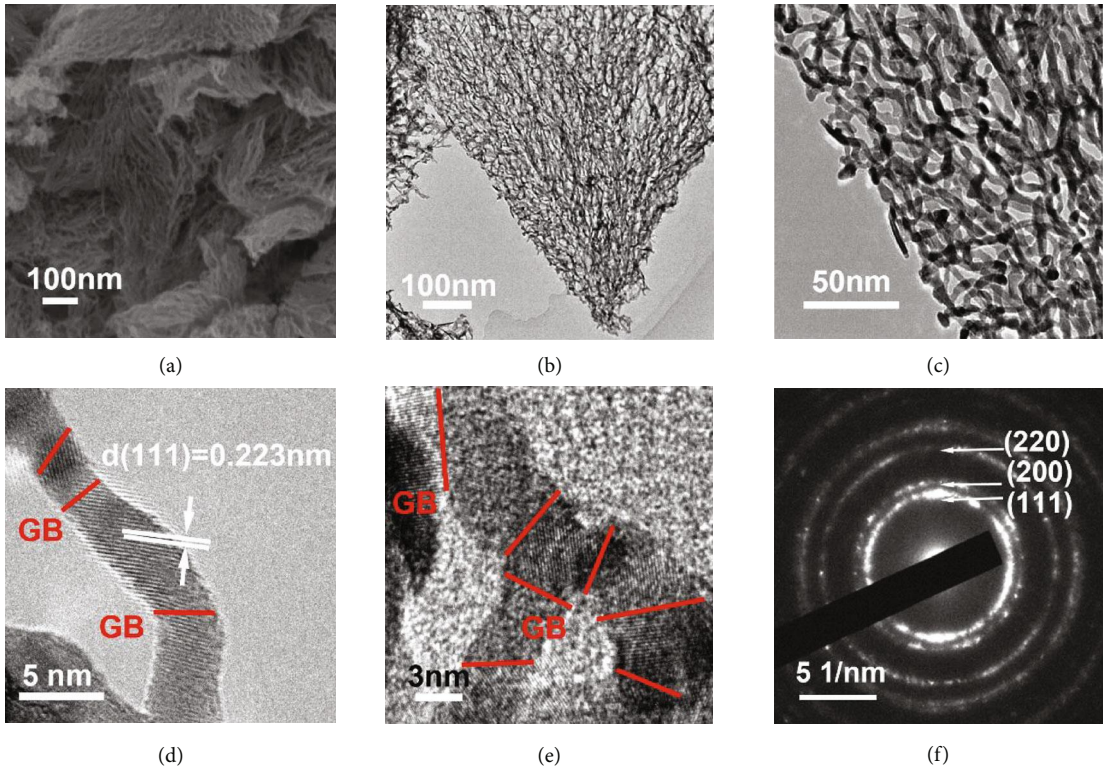

Figure 3: Morphological and structural characterizations of 3D GB-Pt scaffolds. (a) FESEM image of 3D GB-Pt scaffolds. (b, c) TEM images of 3D GB-Pt scaffolds with different magnifications. (d, e) HRTEM images of 3D GB-Pt scaffolds, exhibiting clear grain boundaries and *d*-spacing values of 0.223 nm (Pt (111) lattices). The grain boundaries are marked with red lines in (d) and (e). (f) SAED patterns of 3D GB-Pt scaffolds.

cryogenic treatment, which prevents the infusion between the formed Pt nanocrystalline structures during the reduction process. These results manifest that the appropriate amount of NH_4Cl plays a key role to the formation of 3D grain boundary-enriched Pt scaffolds. To further confirm this hypothesis, two chloroplatinates without ammonium (Na_2PtCl_6 and K_2PtCl_6) were selected to substitute the platinum precursor $(NH_4)_2PtCl_6$ during our fabrication processes. As shown in Figure S14a-c, only Pt nanoparticles were generated after reduction of the fast cryoequilibrium hydrolysates of K_2PtCl_6. If we deliberately added an amount of NH_4Cl into the K_2PtCl_6 system, 3D Pt scaffolds could be formed again (Figure S14d-f and Figure S15). This phenomenon appears again as Na_2PtCl_6 was used as the Pt precursor (Figures S16 and S17). Therefore, the presence of a moderate amount of NH_4Cl is the essence of the production of 3D grain boundary-enriched Pt scaffolds. In this manner, various grain boundary-enriched metal (e.g., Pd) scaffolds could be fabricated via our fast cryogenic treatment with the presence of a NH_4Cl additive, and the detailed characterizations of 3D GB-Pd scaffolds are shown in the Supplementary Materials (Figure S18-S21).

It should be noted that the grain boundary density of the sample can be well controlled through tuning of the hydrolysis equilibrium by adjusting the concentrations of $(NH_4)_2PtCl_6$ solution before fast cryogenic treatment. As shown in Figure S22, a higher concentration of $(NH_4)_2PtCl_6$ leads to an increase of the length of Pt wires. Based on the TEM analysis, we quantitatively measured the average Pt grain length of the GB-Pt scaffolds. It is shown that the average grain length of GB-Pt scaffolds-5 is only 13.2 nm (the grain boundary density of 75.9 μm^{-1}), which is the highest grain boundary density among all the GB-Pt scaffolds samples. (For details, see the Supplementary Materials.) In this manner, the grain boundary density of 3D GB-Pd scaffolds was 64.1 μm^{-1} (Figure S23).

2.3. Structural and Compositional Analysis of 3D GB-Pt Scaffolds. To gain further insight into the crystalline properties of 3D GB-Pt scaffolds, XRD, XPS, and nitrogen adsorption/desorption isotherm were carried out. As revealed in Figure 4(a) and Figures S24 and S25, in the case of 3D GB-Pt scaffolds, there are three prominent XRD peaks at 39.8°, 46.2°, and 67.7°, corresponding to the (111), (200), and (220) planes of face-centered-cubic (fcc) platinum (JCPDS no. 87-0647) [37], respectively, in good accordance with the above HRTEM and SAED analyses. The XPS survey demonstrates that there are only two main species of Pt and O detected in our 3D GB-Pt scaffolds, without other impurities (Figure 4(b) and Figures S26 and S27). N_2 adsorption-desorption data indicates a high specific surface area of 50.6 $m^2\ g^{-1}$, much higher than that of the Pt rods (21.1 $m^2\ g^{-1}$) sample (Figure 4(c)).

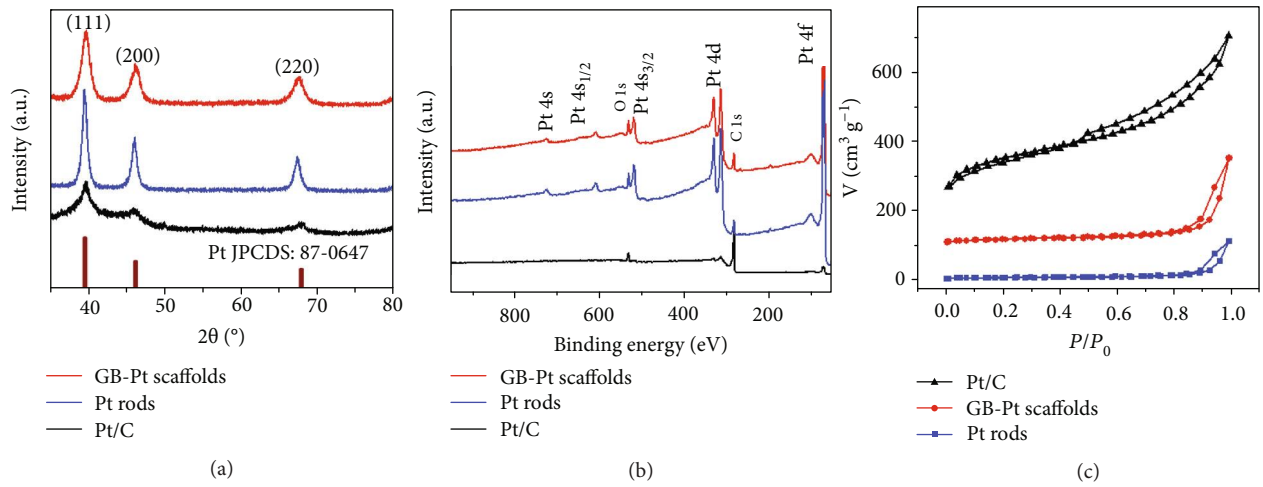

FIGURE 4: Structural characterizations of 3D GB-Pt scaffolds, Pt rods, and commercial Pt/C. (a) XRD patterns demonstrating that all peaks can be indexed to fcc Pt, (b) XPS spectra demonstrating that no other impurity elements were observed, and (c) nitrogen adsorption/desorption isotherm of 3D GB-Pt scaffolds, Pt rods, and Pt/C.

2.4. Electrocatalytic Properties of 3D GB-Pt Scaffolds for Methanol Oxidation. The electrocatalytic activities of 3D GB-Pt scaffolds for MOR were investigated directly via cyclic voltammograms (CVs) in an electrolyte of 0.5 M H_2SO_4 and 1 M methanol. As displayed in Figure 5(a) and Figure S28, a high electrochemically active surface area (ECSA) value of 74.8 m^2 g_{Pt}^{-1} is obtained in the case of GB-Pt scaffolds, much higher than in Pt rods (26.9 m^2 g_{Pt}^{-1}) and Pt/C (35.9 m^2 g_{Pt}^{-1}) (Table S1). Accurately, as shown in Figures 5(b) and 5(c), an ultrahigh peak with current density of 203.8 mA cm^{-2} is achieved, corresponding to 1027.1 mA mg_{Pt}^{-1} for 3D GB-Pt scaffolds in mass activity, much higher than that of the Pt/C sample (345.2 mA mg_{Pt}^{-1}) (Figure S29). Moreover, the onset potential of 3D GB-Pt scaffolds is only 217 mV, much lower than those of Pt rods (257 mV) and the Pt/C catalyst (356 mV). Associated with the above TEM and HRTEM analyses, such high electrocatalytic activities of 3D GB-Pt scaffolds should be attributed to the large presence of grain boundaries of Pt. This can be further demonstrated by the different 3D GB-Pt scaffolds with tunable intensities of grain boundaries, in which their activities are linearly proportional to the densities of grain boundaries of Pt (Figure 5(d)). The electrocatalytic activity of 3D GB-Pt scaffolds obtained at different pH values was also systematically investigated (Figure S30). Among them, 3D GB-Pt scaffolds-pH(7) exhibit a very high value of 1027.1 mA mg_{Pt}^{-1}, much higher than other samples (368.9, 586.9, 485.6, and 166.6 mA mg_{Pt}^{-1} for 3D GB-Pt scaffolds-pH(0), (2), (12), and (14), respectively).

To further investigate the electrocatalytic stability of 3D GB-Pt scaffolds for MOR, we conducted a stability test in 0.5 M H_2SO_4 and 1 M methanol. Remarkably, even after 5000 cycles, there is only 9.8% loss of the initial activity for 3D GB-Pt scaffolds (Figure 5(e)). This value is much lower than that of the Pt/C catalyst (66.5% loss of the activity), clearly confirming the excellent durability of 3D GB-Pt scaffolds for electrocatalytic MOR. To gain insight into the reason of the excellent durability performance of 3D GB-Pt scaffolds, CO-stripping measurement was conducted [38]. As demonstrated in Figure S31, the peak potential of 3D GB-Pt scaffolds is only 0.54 V (vs. SCE), much lower than that of Pt/C (0.61 V vs. SCE), suggesting that 3D GB-Pt scaffolds have an enhanced antipoisoning (CO) property [39]. This should ascribe to the presence of large Pt grain boundaries that can efficiently oxidize the adsorbed CO_{ads} [40]. Furthermore, after durability measurement, both the configurations and grain boundaries of 3D GB-Pt scaffolds were well preserved (Figure S32). The electrochemical impedance spectroscopy (EIS) of the 3D GB-Pt scaffolds, Pt rods, and Pt/C electrocatalysts was carried out to investigate the kinetics of methanol oxidation. As shown in Figures S33 and S34, typical methanol oxidation behaviors catalyzed by the Pt-based catalyst are observed at a series of potentials from 0.1 to 1.0 V [11]. Among them, 3D GB-Pt scaffolds have a much smaller semicircle diameter than Pt rods and Pt/C electrocatalysts at 0.4 V (Figure 5(f)), demonstrating the high methanol oxidation rate of 3D GB-Pt scaffolds [41], in accordance with the electrocatalytic MOR results (Figure 5(b)). In addition, 3D GB-Pd scaffolds also exhibit remarkably high activity of 1117.9 mA mg_{Pd}^{-1} (Figure S35) and good stability (9.0% loss of the initial activity after 5000 CV cycles) towards MOR (Figure S36).

3. Discussion

In summary, grain boundary-enriched platinum scaffolds were produced in large scale via simply reducing fast cryomediated dynamic equilibrium hydrolysates of $(NH_4)_2PtCl_6$. Such plentiful platinum grain boundaries are ascribed to the fast fusion of short platinum nanowires during reduction of the individually and homogeneously dispersed platinum-containing intermediates in the NH_4Cl matrix, which is the essence of the production of grain boundary-enriched Pt scaffolds. These grain boundaries

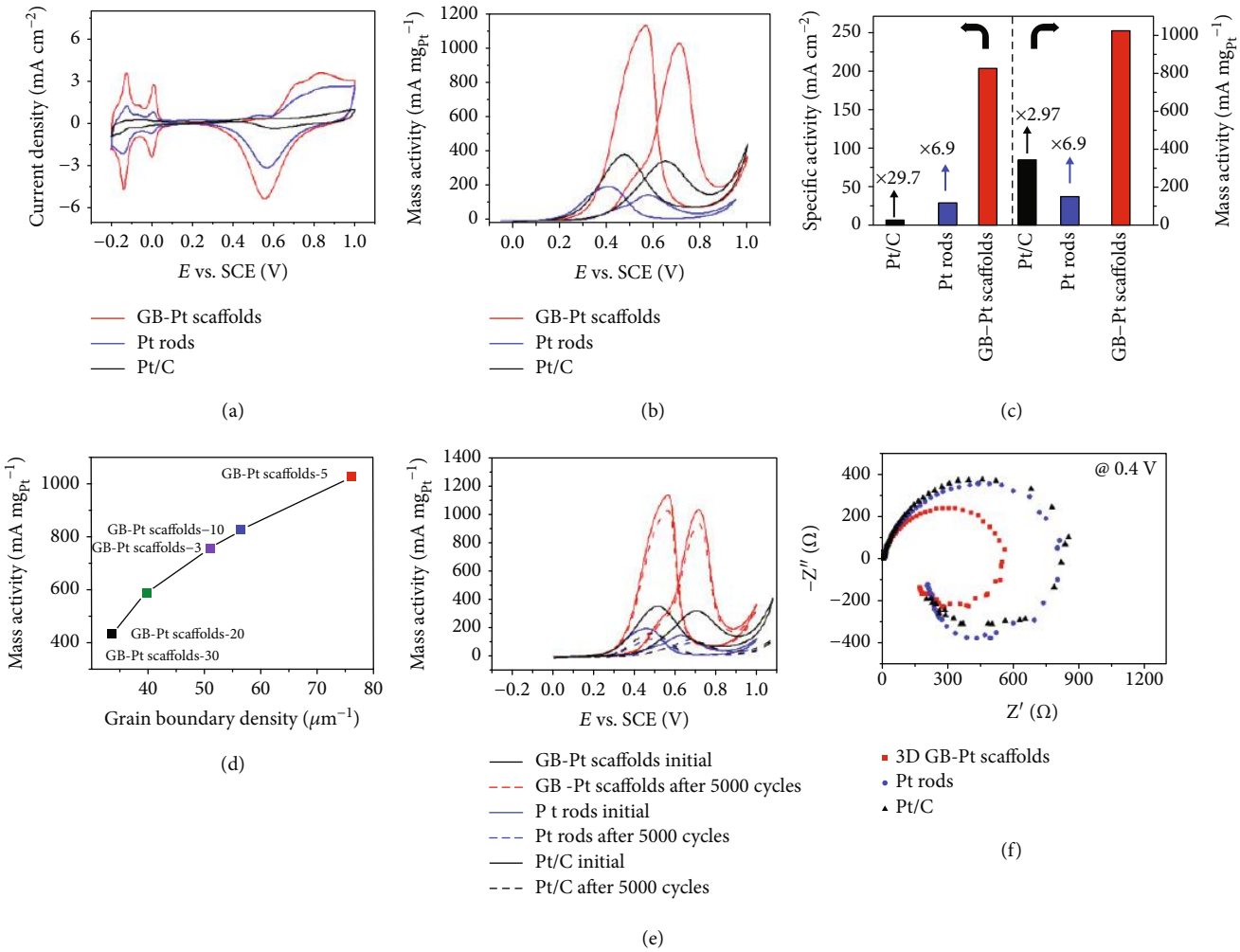

FIGURE 5: Electrocatalytic activities of 3D GB-Pt scaffolds for MOR. (a) Cyclic voltammograms (CVs) tested in 0.5 M H_2SO_4 electrolyte at 10 mV s^{-1}. (b) CVs tested in 0.5 M H_2SO_4 and 1 M methanol electrolyte with 20 mV s^{-1}. (c) Comparative Pt mass activity and specific activity of 3D GB-Pt scaffolds, Pt rods, and Pt/C electrocatalysts. (d) Relationship between grain boundary density and MOR mass activity of 3D GB-Pt scaffolds, showing that the electrocatalytic activities are linearly proportional to the densities of grain boundaries. (e) CVs of 3D GB-Pt scaffolds, Pt rods, and Pt/C before and after 5000 CV cycles, showing an excellent durability of the 3D GB-Pt scaffolds. (f) Nyquist plots of 3D GB-Pt scaffolds, Pt rods, and Pt/C electrocatalysts for methanol oxidation at 0.4 V.

can provide abundant active sites to efficiently catalyze methanol oxidation, with an ultrahigh mass activity of 1027.1 mA mg_{Pt}^{-1} for MOR, much higher than that of commercial Pt/C (345.2 mA mg_{Pt}^{-1}). Moreover, the mass activities of 3D GB-Pt scaffolds are linearly proportional to the densities of grain boundaries of Pt. And these grain boundaries enable oxidization of the adsorbed poisonous CO during the electrocatalytic process, leading to a long stability up to 5000 cycles. We are confident that such a simple synthetic protocol can be extended to produce various grain boundary-enriched metal scaffolds with broad applications for catalysis and sensors.

4. Materials and Methods

4.1. Materials. Ammonium hexachloroplatinate ($(NH_4)_2PtCl_6$), potassium hexachloroplatinate (K_2PtCl_6), sodium hexachloroplatinate (Na_2PtCl_6), and ammonium hexachloropalladate ($(NH_4)_2PdCl_6$) were purchased from Alfa Aesar. Ammonium chloride and sodium chloride were purchased from Beijing Innochem Technology Co., Ltd.

4.2. Synthesis of 3D GB-Pt Scaffolds. For the synthesis of 3D GB-Pt scaffolds, a certain amount of $(NH_4)_2PtCl_6$ was initially added in DI water (10 ml) to form a pale-yellow solution. The solution was stirred for 60 min and then frozen at -196°C in liquid nitrogen for 30 min; after that, the obtained frozen product was further dried under vacuum conditions at -60°C for 48 h, and a three-dimensional yellow foam was obtained. The foam was further reduced at 200°C for 2 h under 10% H_2/Ar gas, generating 3D GB-Pt scaffolds. 3D GB-Pt scaffolds-*X* were fabricated, where *X* represents the amount of $(NH_4)_2PtCl_6$ in the 10 ml solution before fast cryogenic treatment. 3D GB-Pt scaffolds-pH(*Y*) were also fabricated, where *Y* represents the pH value of the $(NH_4)_2PtCl_6$ solution before fast cryogenic treatment.

4.3. Synthesis of Pt Rods. The synthetic procedure of Pt rods was similar to that of 3D GB-Pt scaffolds except that the fast cryogenic treatment was replaced by slow cryogenic treatment (the freezing temperature changed form -196°C to -5°C).

4.4. Synthesis of 3D GB-Pd Scaffolds. The synthetic procedure of 3D GB-Pd scaffolds was similar to that of 3D GB-Pt scaffolds except that the $(NH_4)_2PtCl_6$ was replaced by $(NH_4)_2PdCl_6$, and 5 mg of NH_4Cl should added into the $(NH_4)_2PdCl_6$ solution before fast cryogenic treatment.

4.5. Characterization Methods. Nanostructures and morphologies of all the samples were carried out through FESEM (JEOL-7500) and HRTEM (JEOL, NEM-2100F). Nitrogen sorption isotherms and BET surface area were measured with Quadrasorb at 77 K. The powder X-ray diffraction patterns were conducted by a Rigaku D/max2500PC diffractometer with a Cu Kα radiation over the range 35-80°. XPS data and chemical bonding nature of Pt and O elements were acquired using Thermo Scientific ESCALAB 250Xi X-ray photoelectron spectroscopy (XPS).

4.6. Electrocatalytic Measurements. Electrocatalytic properties of our samples were investigated by using an AutoLab workstation in a three-electrode setup cell. Typically, 3 mg of sample and 80 μl of 5 wt% Nafion solution was dispersed in 1 ml of 4 : 1 *v*/*v* deionized water/ethanol by sonication, forming a black dispersion. Next, 5 μl of the as-prepared dispersion was casted onto a glass carbon electrode 3 mm in diameter as the working electrode. Meanwhile, a saturated calomel electrode (SCE) was applied as the counter electrode and a Pt sheet was applied as the reference electrode. The typical electrochemically active surface area (ECSA) measurement of our samples was tested in nitrogen-saturated 0.5 M H_2SO_4 electrolyte at 10 mV s^{-1}. The MOR electrocatalytic activity was recorded in 0.5 M H_2SO_4 and 1 M methanol electrolyte at 20 mV s^{-1}. For Pd-based catalysts, the MOR electrocatalytic activity was recorded in 1 M KOH and 1 M methanol electrolyte. The chronoamperometry (CA) test was conducted for a period of 1 h at room temperature. The electrochemical impedance spectra (EIS) were recorded at the frequency range from 100000 Hz to 0.01 Hz with an amplitude of 10 mV.

Conflicts of Interest

The authors declare that there are no conflicts of interest regarding the publication of this article.

Authors' Contributions

S. Yang and S. Li conceived and designed the experiments. C. Zhang and H. Huang conducted the experiments. Z. Du, J. Gu, and B. Li recorded the SEM, TEM, XRD, and XPS data. C. Zhang and S. Yang wrote the manuscript.

Acknowledgments

This work was financially supported by the National Science Foundation of China (Nos. 51622203 and 51572007), "Recruitment Program of Global Experts."

Supplementary Materials

Figure S1: photograph of the synthesis process of 3D GB-Pt scaffolds with (a) 0.3 mg/ml, (b) 0.5 mg/ml, (c) 1 mg/ml, (d) 2 mg/ml, and (e) 3 mg/ml of $(NH_4)_2PtCl_6$ solution as the Pt precursor. Figure S2: changes of the electronic absorption spectrum of the $(NH_4)_2PtCl_6$ with a different amount of NaCl, clearly indicating that the $[PtCl_6]^{2-}$ ion undergoes deep hydrolysis with less amount of NaCl. Figure S3: morphological characterizations of the fast cryoequilibrium hydrolysates. (a–c) TEM and HRTEM images of the fast cryoequilibrium hydrolysates (pH(2)) with an inset image of SAED patterns. (d–f) TEM and HRTEM images of the fast cryoequilibrium hydrolysates (pH(7)) with an inset image of SAED patterns. (g–i) TEM and HRTEM images of the fast cryoequilibrium hydrolysates (pH(12)) with an inset image of SAED patterns. Figure S4: (a, e) STEM images and (b–d and f–h) corresponding elemental mapping images of the fast cryoequilibrium hydrolysates. Figure S5: FESEM images of 3D GB-Pt scaffolds-*X*. (a, b) GB-Pt scaffolds-30. (c, d) GB-Pt scaffolds-20. (e, f) GB-Pt scaffolds-10. (g, h) GB-Pt scaffolds-5. (i, j) GB-Pt scaffolds-3. Figure S6: SEM images of the products obtained by hydrogen reduction of fast cryoequilibrium hydrolysate intermediates with different time: (a) 0 min, (b) 40 min, (c) 80 min, and (d) 120 min. Figure S7: TEM images of 3D GB-Pt scaffolds-*X*. (a, b) GB-Pt scaffolds-30. (c, d) GB-Pt scaffolds-20. (e, f) GB-Pt scaffolds-10. (g, h) GB-Pt scaffolds-5. (i, j) GB-Pt scaffolds-3. Figure S8: (a–d) HRTEM images of 3D GB-Pt scaffolds with marked grain boundaries. Figure S9: morphological characterizations of slow cryogenic hydrolysates. (a–c) TEM and HRTEM images of the slow cryoequilibrium hydrolysates (pH(7)). (d–f) TEM and HRTEM images of the slow cryoequilibrium hydrolysates (pH(2)). Figure S10: (a–c) SEM images of Pt rods. Figure S11: (a–c) TEM images of Pt rods. Figure S12: FESEM images of GB-Pt scaffolds derived from hydrogen reduction of fast cryoequilibrium hydrolysates with different pH values. (a–c) 3D GB-Pt scaffolds-pH(0). (d–f) 3D GB-Pt scaffolds-pH(2). (g–i) 3D GB-Pt scaffolds-pH(7). (j–l) 3D GB-Pt scaffolds-pH(12). (m–o) 3D GB-Pt scaffolds-pH(14). Figure S13: TEM images of GB-Pt scaffolds derived from hydrogen reduction of fast cryoequilibrium hydrolysates with different pH values. (a–c) 3D GB-Pt scaffolds-pH(0). (d–f) 3D GB-Pt scaffolds-pH(2). (g–i) 3D GB-Pt scaffolds-pH(7). (j–l) 3D GB-Pt scaffolds-pH(12). (m–o) 3D GB-Pt scaffolds-pH(14). Figure S14: SEM images of reduced fast cryoequilibrium hydrolysates of K_2PtCl_6 without and with additional NH_4Cl. (a-c) SEM images of reduced fast cryoequilibrium hydrolysates of K_2PtCl_6 solution. (d–f) SEM images of reduced fast cryoequilibrium hydrolysates of K_2PtCl_6 and NH_4Cl solution. Figure S15: (a–c) TEM images of reduced

fast cryoequilibrium hydrolysates of K_2PtCl_6 with additional NH4Cl, with marked grain boundaries in (c). Figure S16: SEM images of reduced fast cryoequilibrium hydrolysates of Na_2PtCl_6 without and with additional NH_4Cl. (a–c) SEM images of reduced fast cryoequilibrium hydrolysates of Na_2PtCl_6 solution. (d–f) SEM images of reduced fast cryoequilibrium hydrolysates of Na_2PtCl_6 and NH_4Cl solution. Figure S17: (a–c) TEM images of reduced fast cryoequilibrium hydrolysates of Na_2PtCl_6 with additional NH_4Cl, with marked grain boundaries in (c). Figure S18: FESEM and TEM images of 3D GB-Pd scaffolds. (a, b) FESEM image of 3D GB-Pd scaffolds with different magnifications. (c, d) TEM images of 3D GB-Pd scaffolds with different magnifications. (e) HRTEM images of 3D GB-Pd scaffolds, exhibiting *d*-spacing values of 0.234 nm (Pd (111) lattices). (f) SAED patterns of 3D GB-Pd scaffolds. Figure S19: (a–d) HRTEM images of 3D GB-Pd scaffolds with marked grain boundaries. Figure S20: XRD patterns of the 3D GB-Pd scaffolds and Pd/C. Figure S21: (a) nitrogen adsorption/desorption isotherm of 3D GB-Pd scaffolds. (b) Nitrogen adsorption/desorption isotherm of Pd/C. Figure S22: grain length distribution of the 3D GB-Pt scaffolds. (a–e) Grain length distribution of GB-Pt scaffolds-3, GB-Pt scaffolds-5, GB-Pt scaffolds-10, GB-Pt scaffolds-20, and GB-Pt scaffolds-30, respectively. (f) Average grain length and grain boundary density of the 3D GB-Pt scaffolds. Figure S23: grain length distribution of the 3D GB-Pd scaffolds. Figure S24: XRD patterns of the 3D GB-Pt scaffolds. Figure S25: XRD patterns of the 3D GB-Pt scaffolds prepared from different pH values of the $(NH_4)_2PtCl_6$ solution. Figure S26: XPS spectra of the 3D GB-Pt scaffolds. Figure S27: Pt 4f spectra of the 3D GB-Pt scaffolds, Pt rods, and Pt/C samples. Figure S28: cyclic voltammetry curves of the 3D GB-Pt scaffolds in the 0.5 M H_2SO_4 electrolyte at a sweep rate of 10 mV s^{-1}. Figure S29: electrocatalytic MOR properties of (a) 3D GB-Pt scaffolds and (b) Pt rods and Pt/C catalysts. Figure S30: electrocatalytic MOR properties of the 3D GB-Pt scaffolds-pH(0), (2), (7), (12), and (14). Figure S31: CO tolerance of 3D GB-Pt scaffold and Pt/C catalyst measurement by stripping voltammetry of adsorbed CO, indicating that 3D GB-Pt scaffolds have enhanced antipoisoning (CO) property. Figure S32: (a) TEM and (b) HRTEM images of 3D GB-Pt scaffolds after 5000 cycles. Figure S33: Nyquist plots for the 3D GB-Pt scaffolds, Pt rods, and Pt/C electrocatalysts. (a–c) Nyquist plots for (a) 3D GB-Pt scaffolds, (b) Pt rods, and (c) Pt/C in electrochemical methanol oxidation at different potentials. (d) Nyquist plots of 3D GB-Pt scaffolds, Pt rods, and Pt/C electrocatalysts for methanol oxidation at 0.4 V. Figure S34: (a–c) Nyquist plots of 3D GB-Pt scaffolds, Pt rods, and Pt/C electrocatalysts for methanol oxidation before and after stability test. Figure S35: (a, b) comparative Pd specific activity and mass activity of 3D GB-Pd scaffolds and Pd/C (10 wt%) in 1 M KOH and 1 M methanol electrolyte. Figure S36: CVs of 3D GB-Pd scaffolds before and after 5000 cycles in 1 M KOH and 1 M methanol electrolyte. Table S1: electrochemical surface area (ECSA) of 3D GB-Pt scaffolds, Pt rods, and commercial Pt/C electrocatalysts. *(Supplementary Materials)*

References

[1] M. Escudero-Escribano, P. Malacrida, M. H. Hansen et al., "Tuning the activity of Pt alloy electrocatalysts by means of the lanthanide contraction," *Science*, vol. 352, no. 6281, pp. 73–76, 2016.

[2] H. Wang, S. Xu, C. Tsai et al., "Direct and continuous strain control of catalysts with tunable battery electrode materials," *Science*, vol. 354, no. 6315, pp. 1031–1036, 2016.

[3] D. Larcher and J.-M. Tarascon, "Towards greener and more sustainable batteries for electrical energy storage," *Nature Chemistry*, vol. 7, no. 1, pp. 19–29, 2014.

[4] B. Y. Xia, H. B. Wu, N. Li, Y. Yan, X. W. D. Lou, and X. Wang, "One-pot synthesis of Pt-Co alloy nanowire assemblies with tunable composition and enhanced electrocatalytic properties," *Angewandte Chemie International Edition*, vol. 54, no. 12, pp. 3797–3801, 2015.

[5] J. Suntivich, Z. Xu, C. E. Carlton et al., "Surface composition tuning of Au-Pt bimetallic nanoparticles for enhanced carbon monoxide and methanol electro-oxidation," *Journal of the American Chemical Society*, vol. 135, no. 21, pp. 7985–7991, 2013.

[6] X. Yue, C. He, C. Zhong, Y. Chen, S. P. Jiang, and P. K. Shen, "Fluorine-doped and partially oxidized tantalum carbides as nonprecious metal electrocatalysts for methanol oxidation reaction in acidic media," *Advanced Materials*, vol. 28, no. 11, pp. 2163–2169, 2016.

[7] H.-H. Li, Q.-Q. Fu, L. Xu et al., "Highly crystalline PtCu nanotubes with three dimensional molecular accessible and restructured surface for efficient catalysis," *Energy & Environmental Science*, vol. 10, no. 8, pp. 1751–1756, 2017.

[8] S.-Y. Ma, H. H. Li, B. C. Hu, X. Cheng, Q. Q. Fu, and S. H. Yu, "Synthesis of low Pt-based quaternary PtPdRuTe nanotubes with optimized incorporation of Pd for enhanced electrocatalytic activity," *Journal of the American Chemical Society*, vol. 139, no. 16, pp. 5890–5895, 2017.

[9] Z. Qi, C. Xiao, C. Liu et al., "Sub-4 nm PtZn intermetallic nanoparticles for enhanced mass and specific activities in catalytic electro-oxidation reaction," *Journal of the American Chemical Society*, vol. 139, no. 13, pp. 4762–4768, 2017.

[10] Q. Feng, S. Zhao, D. He et al., "Strain engineering to enhance the electrooxidation performance of atomic-layer Pt on intermetallic Pt_3Ga," *Journal of the American Chemical Society*, vol. 140, no. 8, pp. 2773–2776, 2018.

[11] J. Chang, L. Feng, C. Liu, W. Xing, and X. Hu, "Ni_2P enhances the activity and durability of the Pt anode catalyst in direct methanol fuel cells," *Energy Environmental Science*, vol. 7, no. 5, pp. 1628–1632, 2014.

[12] J. Li, H. M. Yin, X. B. Li et al., "Surface evolution of a Pt–Pd–Au electrocatalyst for stable oxygen reduction," *Nature Energy*, vol. 2, no. 8, article 17111, 2017.

[13] W.-Y. Zhao, B. Ni, Q. Yuan et al., "Highly active and durable $Pt_{72}Ru_{28}$ porous nanoalloy assembled with sub-4.0 nm particles for methanol oxidation," *Advanced Energy Materials*, vol. 7, no. 8, article 1601593, 2017.

[14] N. Erini, V. Beermann, M. Gocyla et al., "The effect of surface site ensembles on the activity and selectivity of ethanol electrooxidation by octahedral PtNiRh nanoparticles," *Angewandte Chemie International Edition*, vol. 56, no. 23, pp. 6533–6538, 2017.

[15] M. Li, Z. Zhao, T. Cheng et al., "Ultrafine jagged platinum nanowires enable ultrahigh mass activity for the oxygen reduction reaction," *Science*, vol. 354, no. 6318, pp. 1414–1419, 2016.

[16] K. Jiang, D. Zhao, S. Guo et al., "Efficient oxygen reduction catalysis by subnanometer Pt alloy nanowires," *Science Advances*, vol. 3, no. 2, article e1601705, 2017.

[17] J. Mao, W. Chen, D. He et al., "Design of ultrathin Pt-Mo-Ni nanowire catalysts for ethanol electrooxidation," *Science Advances*, vol. 3, no. 8, article e1603068, 2017.

[18] M. Luo, Y. Sun, X. Zhang et al., "Stable high-index faceted Pt skin on zigzag-like PtFe nanowires enhances oxygen reduction catalysis," *Advanced Materials*, vol. 30, no. 10, article 1705515, 2018.

[19] Z. Zhang, G. Liu, X. Cui et al., "Crystal phase and architecture engineering of lotus-thalamus-shaped Pt-Ni anisotropic superstructures for highly efficient electrochemical hydrogen evolution," *Advanced Materials*, vol. 30, no. 30, article 1801741, 2018.

[20] L. Bu, N. Zhang, S. Guo et al., "Biaxially strained PtPb/Pt core/shell nanoplate boosts oxygen reduction catalysis," *Science*, vol. 354, no. 6318, pp. 1410–1414, 2016.

[21] L. Ruan, E. Zhu, Y. Chen et al., "Biomimetic synthesis of an ultrathin platinum nanowire network with a high twin density for enhanced electrocatalytic activity and durability," *Angewandte Chemie International Edition*, vol. 52, no. 48, pp. 12577–12581, 2013.

[22] X. Wang, L. Figueroa-Cosme, X. Yang et al., "Pt-based icosahedral nanocages: using a combination of {111} facets, twin defects, and ultrathin walls to greatly enhance their activity toward oxygen reduction," *Nano Letters*, vol. 16, no. 2, pp. 1467–1471, 2016.

[23] B. Cai, R. Hübner, K. Sasaki et al., "Core-shell structuring of pure metallic aerogels towards highly efficient Pt utilization for the oxygen reduction reaction," *Angewandte Chemie International Edition*, vol. 57, no. 11, pp. 2963–2966, 2017.

[24] N. Becknell, Y. Son, D. Kim et al., "Control of architecture in rhombic dodecahedral Pt-Ni nanoframe electrocatalysts," *Journal of the American Chemical Society*, vol. 139, no. 34, pp. 11678–11681, 2017.

[25] S. Li, J. Lai, R. Luque, and G. Xu, "Designed multimetallic Pd nanosponges with enhanced electrocatalytic activity for ethylene glycol and glycerol oxidation," *Energy Environmental Science*, vol. 9, no. 10, pp. 3097–3102, 2016.

[26] A. N. Kuznetsov, P. A. Simonov, V. I. Zaikovskii, V. N. Parmon, and E. R. Savinova, "Temperature effects in carbon monoxide and methanol electrooxidation on platinum–ruthenium: influence of grain boundaries," *Journal of Solid State Electrochemistry*, vol. 17, no. 7, pp. 1903–1912, 2013.

[27] C. H. Chen, K. E. Meadows, A. Cuharuc, S. C. S. Lai, and P. R. Unwin, "High resolution mapping of oxygen reduction reaction kinetics at polycrystalline platinum electrodes," *Physical Chemistry Chemical Physics*, vol. 16, no. 34, pp. 18545–18552, 2014.

[28] B. Y. Xia, H. B. Wu, Y. Yan, X. W. (. D.). Lou, and X. Wang, "Ultrathin and ultralong single-crystal platinum nanowire assemblies with highly stable electrocatalytic activity," *Journal of the American Chemical Society*, vol. 135, no. 25, pp. 9480–9485, 2013.

[29] H. Huang, K. Li, Z. Chen et al., "Achieving remarkable activity and durability toward oxygen reduction reaction based on ultrathin Rh-doped Pt nanowires," *Journal of the American Chemical Society*, vol. 139, no. 24, pp. 8152–8159, 2017.

[30] A. B. Bel'skaya, T. I. Gulyaeva, A. B. Arbuzov, V. K. Duplyakin, and V. A. Likholobov, "Interaction between Pt(IV) and Pd(II) chloro complexes in solution and on the γ-Al_2O_3 surface," *Kinetics and Catalysis*, vol. 51, no. 1, pp. 105–112, 2010.

[31] X. Chen, W. Chu, L. Wang, and Z. Wu, "Geometry of Pt(IV) in H_2PtCl_6 aqueous solution: an X-ray absorption spectroscopic investigation," *Journal of Molecular Structure*, vol. 920, no. 1-3, pp. 40–44, 2009.

[32] Y. Chen, T. Yang, H. Pan et al., "Photoemission mechanism of water-soluble silver nanoclusters: ligand-to-metal–metal charge transfer vs strong coupling between surface plasmon and emitters," *Journal of the Amercian Chemical Society*, vol. 136, no. 5, pp. 1686–1689, 2014.

[33] A. Siani, K. R. Wigal, O. S. Alexeev, and M. Amiridis, "Synthesis and characterization of Pt clusters in aqueous solutions," *Journal of Catalysis*, vol. 257, no. 1, pp. 5–15, 2008.

[34] A. C. Tsipis and I. N. Karapetsas, "Accurate prediction of ^{195}Pt-NMR chemical shifts for hydrolysis products of $[PtCl_6]^{2-}$ in acidic and alkaline aqueous solutions by non-relativistic DFT computational protocols," *Journal of Coordination Chemistry*, vol. 68, no. 21, pp. 3788–3804, 2015.

[35] K. Tang, X. Wang, Q. Li, and C. Yan, "High edge selectivity of in situ electrochemical Pt deposition on edge-rich layered WS_2 nanosheets," *Advanced Materials*, vol. 30, no. 7, article 1704779, 2018.

[36] W. Wang, F. Lv, B. Lei, S. Wan, M. Luo, and S. Guo, "Tuning nanowires and nanotubes for efficient fuel-cell electrocatalysis," *Advanced Materials*, vol. 28, no. 46, pp. 10117–10141, 2016.

[37] H. Wang, W. Luo, L. Zhu et al., "Synergistically enhanced oxygen reduction electrocatalysis by subsurface atoms in ternary PdCuNi alloy catalysts," *Advanced Functional Materials*, vol. 28, no. 15, article 1707219, 2018.

[38] L. Feng, K. Li, J. Chang, C. Liu, and W. Xing, "Nanostructured PtRu/C catalyst promoted by CoP as an efficient and robust anode catalyst in direct methanol fuel cells," *Nano Energy*, vol. 15, pp. 462–469, 2015.

[39] H. Kwon, M. Kabiraz, J. Park et al., "Dendrite-embedded platinum–nickel multiframes as highly active and durable electrocatalyst towards the oxygen reduction reaction," *Nano Letters*, vol. 18, no. 5, pp. 2930–2936, 2018.

[40] C. Wang, X. Sang, J. T. L. Gamler, D. P. Chen, R. R. Unocic, and S. E. Skrabalak, "Facet-dependent deposition of highly strained alloyed shells on intermetallic nanoparticles for enhanced electrocatalysis," *Nano Letters*, vol. 17, no. 9, pp. 5526–5532, 2017.

[41] R. Lin, X. Cai, H. Zeng, and Z. Yu, "Stability of high-performance Pt-based catalysts for oxygen reduction reactions," *Advanced Materials*, vol. 30, no. 17, article 1705332, 2018.